

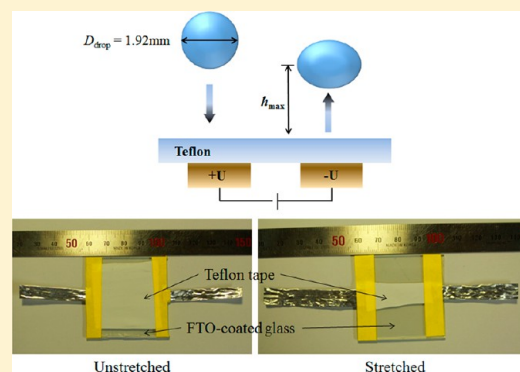
Dynamic Electrowetting-on-Dielectric (DEWOD) on Unstretched and Stretched Teflon

Min Wook Lee,[†] Sanjay S. Lathe,[†] Alexander L. Yarin,^{*,†,‡} and Sam S. Yoon^{*,†}[†]School of Mechanical Engineering, Korea University, Seoul 136-713, Korea[‡]Department of Mechanical and Industrial Engineering, University of Illinois at Chicago, Chicago, Illinois 60607-7022, United States

S Supporting Information

ABSTRACT: Dynamic electrowetting-on-dielectric (DEWOD) of the unstretched and stretched Teflon is reported in the experiments with water drop impact and rebound. We explore experimentally and theoretically the situation with the capacitance different from the standard static electrowetting. Deionized water drops impact onto either an unstretched hydrophobic Teflon surface or Teflon stretched up to 250% strain normally to the impact direction. The surface roughness of the unstretched Teflon increased after stretching from 209.9 to 245.6 nm resulting in the increase in the equilibrium water contact angle from $96 \pm 4^\circ$ to $147 \pm 5^\circ$, respectively. The electric arrangement used in the drop impact experiments on DEWOD results in a dramatically reduced capacitance and requires a much higher voltage to observe EW in comparison with the standard static case of a drop deposited on a dielectric layer and attached to an electrode.

In the dynamic situation we found that as the EW sets in it can greatly reduce the superhydrophobicity of the unstretched and stretched Teflon. At 0 kV, the water drop rebound height (h_{\max}) is higher for the stretched Teflon ($h_{\max} \approx 5.13$ mm) and lower for the unstretched Teflon ($h_{\max} \approx 4.16$ mm). The EW response of unstretched Teflon is weaker than that of the stretched one. At the voltage of 3 kV, the water drop sticks to the stretched Teflon without rebound, whereas water drops still partially rebound ($h_{\max} \approx 2.8$ mm) after a comparable impact onto the unstretched Teflon. We found a sharp dynamic EW response for the stretched Teflon. The contact angle of deionized water ranged from $147 \pm 5^\circ$ (superhydrophobic) to $67 \pm 5^\circ$ (partially hydrophilic) by applying external voltage of 0 and 3 kV, respectively. Dynamic electrowetting introduced in this work for the first time can be used to control spray cooling, painting, and coating and for drop transport in microfluidics.



1. INTRODUCTION

Wettability of solid surfaces with liquids is of great importance in fundamental research and practical applications of adhesion and micro- and nanofluidics.^{1–3} Control of surface wettability by application of external stimuli has drawn significant attention due to a wide range of potential applications. Among various methods for wettability switching, electrowetting (EW) or electrowetting-on-dielectric (EWOD) is arguably one of the most flexible methods to actively control liquid wettability on partially wettable or completely nonwettable surfaces. EW is an electrically induced alteration in materials wettability and has long been known to affect the equilibrium contact angle of drops without changing the chemical composition of the contacting phases.^{2,4} EW results from the reduction in the solid–liquid interfacial energy due to the free charges (ions) accumulating at the dielectric surface when voltage is applied. In turn, the equilibrium contact angle of drops on such dielectric surfaces is affected according to the Young–Lippmann equation, and thus the surface wettability. The apparent equilibrium contact angle can be dramatically altered (often by 50% or more), which has dynamic connotations as well. Therefore, EW offers an excellent alternative for moving

tiny amounts of liquid over hydrophobic surfaces or making them wettable. The effect is precise, repeatable and rapid, making EW a desirable method for manipulating small drops on a surface. Drop manipulation by EW has very useful diverse applications such as digital microfluidics,⁵ electronic displays,⁶ paint drying,⁷ responsive cooling,⁸ adjustable focusing lenses,⁹ and so on.^{10,11} Recent needs for the construction of low-power and efficient EW systems have triggered studies aimed at the mechanism and limitations of EW. The control over the wetting properties of the solid surfaces by EW already has numerous practical applications, yet many aspects of electrowetting behavior are not fully understood. The main difficulty encountered in the static electrowetting is that, after some initial decrease in contact angle, even very large external voltages fail to achieve complete wetting.^{2,12} Several complementary hypotheses have been advanced in that respect, such as dielectric charging,¹³ asymmetric (polarity dependent) electrowetting responses,¹⁴ gas ionization in the vicinity of the contact

Received: February 21, 2013

Published: May 24, 2013

line, contact line instability,¹⁵ droplet resistance,¹² and saturation phenomena.¹⁶

Numerous EW phenomena on micro/nanostructured surfaces involve an enormous change in contact angle and a fast dynamic tuning of the wetting.^{17–20} Generally, wetting behavior is strongly dependent on both surface chemistry (i.e., surface energy) and surface topography (i.e., surface roughness). Superhydrophobic surfaces have been produced mainly in two ways: (i) by creating a rough structure on a hydrophobic surface and (ii) by modifying a rough surface by a material with low surface free energy. For water to wet the superhydrophobic surfaces, external work has to be done to overcome the energy barrier to achieve the transition from the superhydrophobic to hydrophilic state.^{21–26} The EW method offers a powerful, nondestructive, on-demand, and selective way to achieve this. For example, when a liquid drop is placed on a superhydrophobic surface, it stays at the top of the roughness, leading to a small contact area, a large contact angle ($>150^\circ$), and a small roll-off angle (the Cassie–Baxter state).²⁷ Once a voltage is applied, the drop is impaled through the surface texture leading to a contact angle lower than 150° and a high roll-off angle (the Wenzel state).²⁸ It was demonstrated that the use of EW can switch surface wetting properties from the superhydrophobic to nearly completely superhydrophilic.¹⁷ That was achieved by fabricating nanopillars with a diameter of 350 nm and a height of 7 μm by dry etching a Si wafer. Each pillar had a conductive core of Si covered by a thermally grown insulating SiO layer and a hydrophobic top coating. Surfaces can be efficiently made wettable and water pumped through superhydrophobic aligned multiwalled nanotube membranes by application of a small EW voltage.¹⁸ The Cassie–Baxter-to-Wenzel transition by EW was demonstrated on the nanocomposite superhydrophobic surface prepared using spherical amorphous carbon nanoparticles (~ 100 nm thick) capped on carbon nanotubes.¹⁹ Behavior of water drops on aligned carbon nanotube surfaces under the influence of an EW voltage was experimentally investigated, and the limits of contact angle change on such surfaces were established.²⁰

In EWOD devices, the applied electric field is confined in the dielectric layer, so that EW is determined by the geometrical parameters and dielectric permittivity of the dielectric. The main requirement for an efficient EW is the low contact angle hysteresis on the hydrophobic dielectric layer in conjunction with high initial contact angle. One of the most widely used materials relevant to EW is poly(tetrafluoroethylene) (PTFE), i.e., Teflon. It is reported that flat fluoropolymer Teflon reveals the equilibrium contact angle of water of around $108 \pm 2^\circ$.²⁹ A further increase in the equilibrium contact angle of flat Teflon is preferable for most microfluidic devices, since it will not only facilitate drop motion but also extend the functional range of the contact angle. An easy and effective method to prepare superhydrophobic Teflon is to change the density of the fibrous crystals by stretching.

In the present research work, we report the dynamic electrowetting-on-dielectric (DEWOD) performance of unstretched (hydrophobic) and stretched (superhydrophobic) Teflon on FTO substrates. We report for the first time in the literature, the electrowetting effect associated with water drop impact and bouncing, the situation significantly different from standard EW phenomena with sessile drops attached to an electrode. Section 2 describes the experiment and section 3 the theory. The results are exposed and discussed in section 4. Conclusions are drawn in section 5.

2. EXPERIMENTAL SETUP

The commercially available Teflon tape was selected as the dielectric material for DEWOD experiments. The Teflon tape was carefully cut into 50–60 mm (length) \times 50–52 mm (width) \times 100 μm (thickness) pieces. Given the ductile nature of Teflon, the Teflon pieces were stretched to different strains [strain = $(L - L_0)/L_0 \times 100$ (%), where L_0 is the initial length and L is the stretched length] of 50, 100, 150, 200, and 250% (the strain variance was $\pm 10\%$) at a velocity of 50 mm/min at room temperature ($\sim 20^\circ\text{C}$). The thickness of the unstretched Teflon was 100 μm , whereas after stretching to 200%, the thickness diminished to 70 μm . The unstretched and stretched Teflon pieces were fixed on FTO-coated glass substrate as shown in the lower panel in Figure 1 (air bubbles between Teflon and FTO were carefully

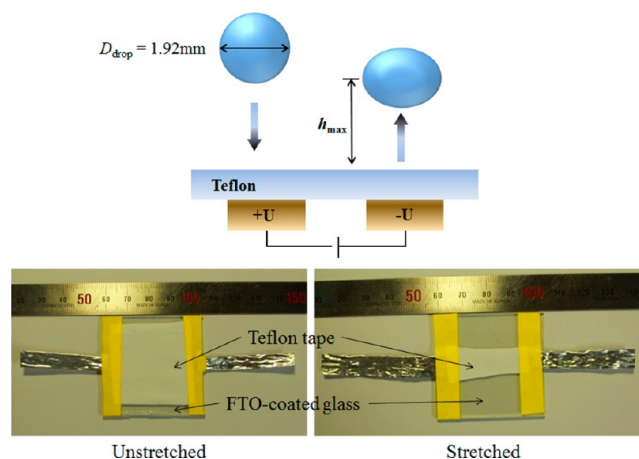


Figure 1. Dynamic electrowetting experiment with drop impact onto Teflon layer. The upper panel shows the sketch and the lower one the photographic images of the setup.

removed) and used for static and dynamical drop impact measurement (with and without EW voltage applied), as well as for SEM and AFM observations.

The EW experiments were carried on the unstretched and stretched Teflon at three different locations on each sample to ensure repeatability. The EW measurements were carried out in the following way: the voltage between 0 and 6 kV was applied by the High Voltage supplier (EL20P2, Glassman) directly to the FTO substrate on which either unstretched or stretched Teflon was fixed. The equilibrium contact angle (ECA) was measured without voltage applied and in static EW experiments. The average ECA value was adopted by measuring at five different positions on the same sample. DI water was supplied to a stainless-steel nozzle (EFD, inner and outer diameters of 100 and 240 μm , respectively) by a syringe pump (KDS Legato 100) at a flow rate of 0.4 mL/min. Spherical drops 1.92 mm in diameter were generated and dripped under gravity onto the substrate. The impact velocity was ~ 62 cm/s. The distance between the nozzle tip and the substrate was fixed at $h = 5$ cm. A high-speed camera (Vision Research, Inc., Phantom 7.3) with zoom lens (1.56 $\mu\text{m}/\text{pixel}$) and LED lamp (50 W) captured the magnified images of ejected DI water drops. In recording the side views, the camera was aligned at the same vertical level as that of the substrate. The error in measuring the locations of points at the drop surface was less than 5° . Snapshots were taken at an interval of $\Delta t = 45$ μs . All measurements and experiments were performed at room temperature. The relative dielectric permittivity of the unstretched and stretched Teflon samples was taken as in the literature as $\epsilon = 2.1$. The surface morphology of the unstretched and stretched Teflon was characterized by scanning electron microscope (SEM; S5000, Hitachi, Ltd.). Surface topography, as well as surface roughness, was measured by atomic force microscope (AFM; Park Systems XE-100) in tapping mode.

3. THEORETICAL MODEL

Electrowetting phenomena arise due to the change of the equilibrium contact angle when voltage V is applied. In standard electrowetting experiments a sessile drop is located on a dielectric substrate and attached to an electrode. When potential difference V exists between the bottom of the dielectric layer and the drop, its equilibrium contact angle depends on V and is given by the Young–Lippmann formula^{2,30}

$$\cos \theta_{eV} = \cos \theta_{e0} + \frac{C_s}{2\gamma} V^2 \quad (1)$$

where θ_{eV} and θ_{e0} are the equilibrium contact angles when voltage V is applied, or no voltage is applied, respectively, and γ is the surface tension of liquid. In addition, the capacitance C_s of the dielectric layer of thickness d in the standard EW experiment with sessile drop is given as

$$C_s = \frac{\epsilon_0 \epsilon_d}{d} \quad (2)$$

where SI units are used, and ϵ_0 and ϵ_d are the dielectric permittivity of vacuum and the relative dielectric permittivity of the dielectric layer underneath the drop.

According to eq 1, at a nonzero voltage V , the equilibrium contact angle of a drop diminishes, which means that it is stretched over the dielectric layer. This stems from the fact that the counterions always present in water almost immediately create the Stern layer at the dielectric surface when voltage is applied, which reduces the interfacial energy of the solid/liquid interface, and thus affects the horizontal force balance expressed by the Young equation, which transforms into eq 1.

However, in the present work a dynamic, rather than a static, situation corresponding to drop impact is involved, as sketched in the upper panel in Figure 1.

A drop of a volume-equivalent radius R_e rapidly spreads after a normal impact at the surface and the maximum spread-out radius a_i of the liquid footprint at the surface is given by the following expression^{31,32}

$$\frac{a_i}{R_e} = 0.61 \left(\frac{We}{Oh} \right)^{0.166} \quad (3)$$

where the Weber and Ohnesorge numbers We and Oh are defined as

$$We = \frac{2\rho R_e V_0^2}{\gamma}, \quad Oh = \frac{\mu}{(2\rho\gamma R_e)^{1/2}} \quad (4)$$

with ρ and μ being liquid density and viscosity, respectively, and V_0 the impact velocity. It is emphasized that eq 3 is valid for dynamic rather than wettability-driven drop spreading and therefore does not include the contact angle. The following values of the dimensionless groups are typical of the present experiments: $We = 10$ and $Oh = 0.004$.

Due to the fact that spread-out drops are subjected to surface tension and the tendency to restore the equilibrium contact angle, receding motion sets in. After a sufficiently strong impact, this motion can even result in drop bouncing due to the significant inertia and low viscous dissipation,³¹ as sketched in the upper panel in Figure 1. (It is emphasized that the ratio of the kinetic energy to viscous dissipation is of the order of the impact Reynolds number $Re = \rho 2R_e V_0 / \mu = We^{1/2} / Oh$ which is close to 828, and thus dissipation is negligible in the present case.) These phenomena proceed on the scale of the order of

$\tau_H = 10\text{--}100$ ms. The hydrodynamic time scale τ_H is much longer than the charge relaxation time $\tau_C = \epsilon_0 \epsilon / \sigma_e$, with σ_e being the electric conductivity of liquid, since τ_C is of the order of $1 \mu\text{s}$ (ref 33). Since $\tau_C \ll \tau_H$, the counterions arrive at the surface of the polarized dielectric underneath the drop almost immediately, and the electric situation at the drop/dielectric interface during the spreading and receding stages does not differ from that in the standard static electrowetting experiment.

However, the electric connection of the dielectric layer depicted in Figure 1 is different from the one in the standard static electrowetting, and thus the capacitance given by eq 2 is inapplicable. To calculate the capacitance corresponding to Figure 1, consider planar electrostatic problem depicted in Figure 2. We use complex variable $z = x + iy$, where i is the imaginary unit.

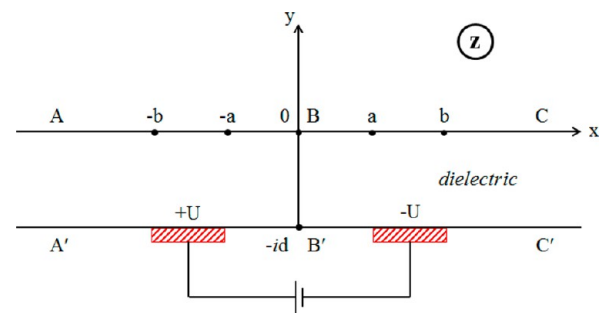


Figure 2. Planar electrostatic problem: complex z -plane corresponding to the dielectric layer $ABCC'B'A'$.

The strip $ABCC'B'A'$ corresponding to the dielectric layer in Figure 2 is mapped onto the upper half-plane in the complex plane $t = \xi + i\eta$ by the following conformal mapping function

$$z = -\frac{d}{\pi} \ln t \quad (5)$$

such that point A is mapped to $t = \infty$, point B' to $t = 1$, and point C' to $t = 0$, which is depicted in Figure 3. It is emphasized

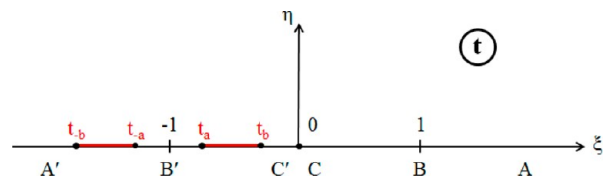


Figure 3. Complex upper half-plane corresponding to the dielectric domain of Figure 2.

that a drop would occupy in Figure 2 a domain in the upper half-plane $y > 0$, which is much larger than the thickness of the dielectric layer d , as well as the interelectrode distance $2a$, or the electrode size $b - a$. We are interested in the formation of the Debye layer at the drop bottom in contact with the dielectric layer at $y = 0$. Since the thickness of the Debye layer is on the 10 nm scale (ref 34), while the sizes a , b , and d are on the 100 μm scale, and the drop size is on the 1 mm scale, one can effectively assume that liquid would occupy the entire upper half-plane $y > 0$ and the Debye layer stretches over $-\infty < x < \infty$.

According to Figure 2, the boundaries of the left-hand side electrode raised to potential U correspond to $z_{-b} = -b - id$ and

$z_{-a} = -a - id$, whereas the boundaries of the right-hand side electrode at potential $-U$ correspond to $z_a = a - id$ and $z_b = b - id$ (note that $b > a$). According to eq 5, these boundaries are mapped to $t_{-b} = -\exp(\pi b/d)$, $t_{-a} = -\exp(\pi a/d)$, $t_a = -\exp(-\pi a/d)$ and $t_b = -\exp(-\pi b/d)$, respectively, as shown in Figure 3. Conformal mapping of eq 5 is equivalent to the following coordinate transformation

$$\xi = \exp\left(-\frac{\pi x}{d}\right) \cos\left(\frac{\pi y}{d}\right), \quad \eta = -\exp\left(-\frac{\pi x}{d}\right) \sin\left(\frac{\pi y}{d}\right) \quad (6)$$

The electric potential φ in the dielectric domains in Figures 2 and 3 is found from the Laplace equation having the similar form due to the conformal mapping, namely

$$\frac{\partial^2 \varphi}{\partial x^2} + \frac{\partial^2 \varphi}{\partial y^2} = 0 \quad (\text{in } z), \quad \frac{\partial^2 \varphi}{\partial \xi^2} + \frac{\partial^2 \varphi}{\partial \eta^2} = 0 \quad (\text{in } t) \quad (7)$$

At the domain boundary, $\varphi = 0$ everywhere except the electrodes, where $\varphi = U$ at the left-hand side electrode and $\varphi = -U$ at the right-hand side electrode. The solution of the Laplace equation in the upper half-plane t is given by Poisson's integral formula,³⁵ which for the present boundary conditions yields

$$\varphi(\xi, \eta) = \frac{\eta U}{\pi} \left[\int_{t_{-b}}^{t_{-a}} \frac{d\zeta}{(\zeta - \xi)^2 + \eta^2} - \int_{t_a}^{t_b} \frac{d\zeta}{(\zeta - \xi)^2 + \eta^2} \right] \quad (8)$$

where ζ is a dummy variable.

Evaluating the elementary integrals in eq 8, and returning to the coordinates x and y using eq 6, we arrive at the following expression for the potential

$$\varphi(x, y) = \frac{U}{\pi} \left[\arctan\left(\frac{t_{-a} - \xi}{\eta}\right) - \arctan\left(\frac{t_{-b} - \xi}{\eta}\right) - \arctan\left(\frac{t_b - \xi}{\eta}\right) + \arctan\left(\frac{t_a - \xi}{\eta}\right) \right] \quad (9)$$

An example of the potential field (9) is shown in Figure 4.

Calculating the derivative $\partial\varphi/\partial y$ at $y = 0$ using eq 9, we can find the surface density of the free charges σ_{ion} on the conducting side (counterions accumulated at the drop bottom) in contact with the top side of the dielectric as

$$\begin{aligned} \sigma_{\text{ion}} &= \epsilon_0 \epsilon \frac{\partial \varphi}{\partial y} \bigg|_{y=0} \\ &= \frac{\epsilon_0 \epsilon}{d} 2U e^{-\pi x/d} [\cosh(\pi b/d) - \cosh(\pi a/d)] \\ &\quad \times \frac{(1 - e^{-2\pi x/d})}{[e^{-2\pi x/d} + 1 + 2e^{-\pi x/d} \cosh(\pi b/d)][e^{-2\pi x/d} + 1 + 2e^{-\pi x/d} \cosh(\pi a/d)]} \end{aligned} \quad (10)$$

The surface density of the free charges predicted by eq 10 and rendered dimensionless as $S = \sigma_{\text{ion}} / \{2U(\epsilon_0 \epsilon/d)[\cosh(\pi b/d) - \cosh(\pi a/d)]\}$ is illustrated in Figure 5. It shows that anions are located at the drop bottom part above the positive electrode (cf. Figure 2), i.e., at $x < 0$, whereas cations are located at the drop bottom part above the negative electrode, i.e., at $x > 0$.

If we assume sufficiently small drop size, $2\pi x/d < 1$, the latter expression is simplified as

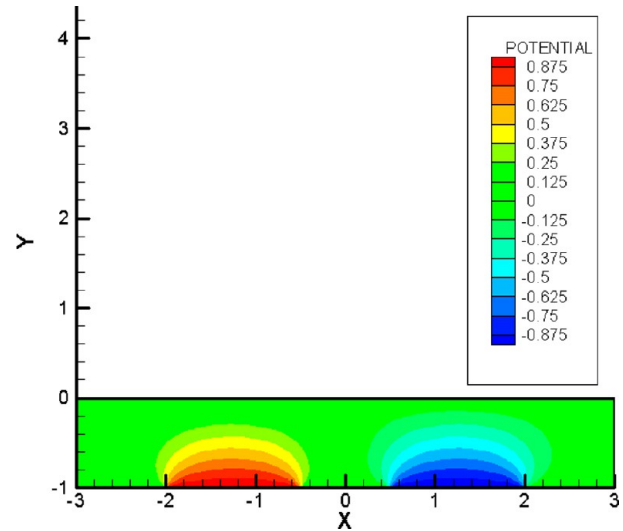


Figure 4. Potential distribution according to eq 9. Potential φ is rendered dimensionless by U , coordinates x and y by the dielectric layer thickness d . The following electrode parameters are used: $a/d = 0.5$ and $b/d = 2$.

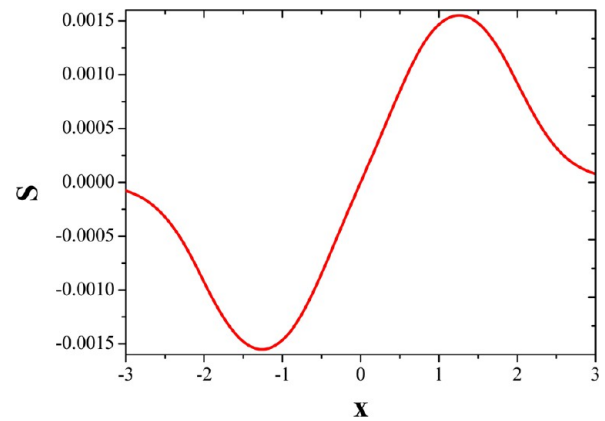


Figure 5. Surface density of the free charges at $a/d = 0.5$ and $b/d = 2$.

$$\sigma_{\text{ion}} = \frac{\epsilon_0 \epsilon}{d} U \frac{[\cosh(\pi b/d) - \cosh(\pi a/d)]}{[1 + \cosh(\pi b/d)][1 + \cosh(\pi a/d)]} \frac{\pi x}{d} \quad (11)$$

and, correspondingly, the electric energy stored in the drop bottom becomes

$$E_{\text{el}} = -\frac{\epsilon_0 \epsilon}{d} U^2 \frac{[\cosh(\pi b/d) - \cosh(\pi a/d)]}{[1 + \cosh(\pi b/d)][1 + \cosh(\pi a/d)]} \frac{\pi |x|}{d} \quad (12)$$

The electric energy stored per unit area of the drop bottom found from eq 12 then becomes

$$\begin{aligned} E_{\text{el}} &= -\frac{\epsilon_0 \epsilon}{d} U^2 \frac{[\cosh(\pi b/d) - \cosh(\pi a/d)]}{[1 + \cosh(\pi b/d)][1 + \cosh(\pi a/d)]} \frac{\pi a_i}{d} \\ &\approx -\frac{\epsilon_0 \epsilon}{d} 4(e^{-\pi a/d} - e^{-\pi b/d}) \frac{\pi a_i}{d} \frac{U^2}{2} \end{aligned} \quad (13)$$

where we used the fact that $b/d > a/d$ and assumed that these ratios are sufficiently larger than 1. Equation 13 shows that, in the drop impact experiments, the “static” equations for the equilibrium contact angle (eqs 1 and 2) are replaced by the following “dynamic” equations for the unstretched Teflon

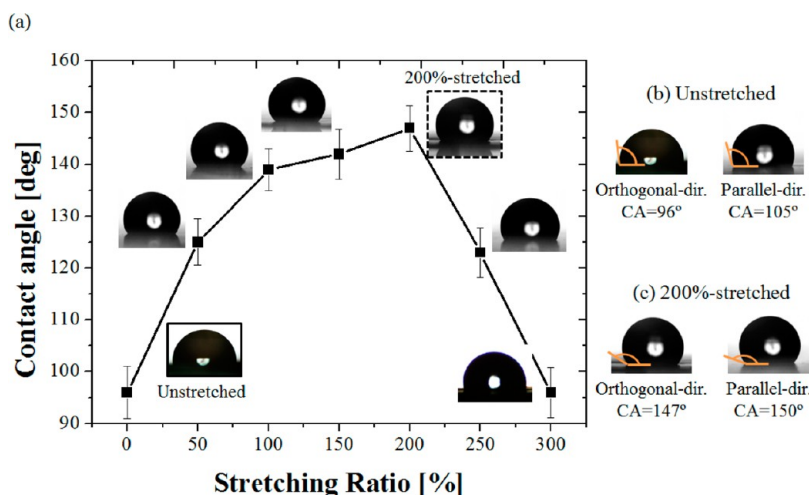


Figure 6. (a) Static water contact angle (SWCA) as a function of the stretching ratio of Teflon tape. The insets show the corresponding optical images of the water drops observed orthogonally to the direction of the main surface ridges; SWCA of the unstretched Teflon is $96 \pm 4^\circ$, whereas of the 200%-stretched one, $147 \pm 5^\circ$. The average ECA values were obtained by measuring at five different positions on the same sample, and the variance is reflected by the error bars. (b) Contact angle of a water drop on the unstretched surface observed orthogonally to the direction of surface ridges and parallel to them. The left-hand side image corresponds to the image of the drop on the unstretched Teflon surrounded by a small rectangular solid frame in panel (a). (c) Contact angle of a water drop on the 200%-stretched surface observed orthogonally to the direction of surface ridges and parallel to them. The left-hand side image corresponds to the image of the drop on the 200%-stretched Teflon surrounded by a small rectangular dashed frame in panel (a).

$$\cos \theta_{eV} = \cos \theta_{e0, \text{unstretched}} + \frac{C_d}{2\gamma} V^2 \quad (14)$$

where $V = 2U$, and the capacitance in the present experiment is given by

$$C_d = \frac{\epsilon_0 \epsilon}{d} (e^{-\pi a/d} - e^{-\pi b/d}) \frac{\pi a_i}{d} \quad (15)$$

Since $b/d > a/d$ and both ratios are expected to be larger than 1, $C_d \ll C_s$, as the comparison of eqs 2 and 15 shows. Therefore, in the drop impact experiments the voltage values corresponding to the visible electrowetting effect should be significantly higher than in the standard static experiments.

In the case of stretched Teflon, one can expect additional surface roughness will appear, as the experimental data in section 4 (Figures 7 and 8) shows. Therefore, when calculating the chemical and electric energy of the drop bottom, one should account for the increased effective surface area. Then, eq 14 is replaced by the following one

$$\cos \theta_{eV} = \cos \theta_{e0, \text{stretched}} + \frac{C_d}{2\gamma} r V^2 \quad (16)$$

In eq 16 the factor r which expresses the ratio of the real surface area of the drop bottom to the projected one is found according to the Wenzel equation as

$$r = \frac{\cos \theta_{0, \text{stretched}}}{\cos \theta_{0, \text{unstretched}}} \quad (17)$$

It is emphasized that eqs 14–17 imply that during drop impact water easily penetrates all of the grooves and cracks at the surface; that is, the Wenzel state is realized in the spread-out wet spot, as it was demonstrated in refs 22–26.

At the moment of the maximum spread-out the restoring force F_r acting at the drop is applied at the contact line and equal to

$$F_r = \gamma (\cos \theta_i - \cos \theta_{eV}) 2\pi a_i \quad (18)$$

where the spread-out contact angle θ_i is found below.

If we approximate the spread-out drop shape as a spherical segment of radius R_i , the latter is equal to

$$R_i = \frac{4^{1/3} R_e}{[(1 - \cos \theta_i)^2 (2 + \cos \theta_i)]^{1/3}} \quad (19)$$

due to the mass conservation.

On the other hand, due to the geometric considerations

$$a_i = R_i \sin \theta_i \quad (20)$$

and thus, according to eqs 3, 19, and 20, we arrive at the following equation which determines the spread-out contact angle θ_i resulting from drop impact

$$\frac{4^{1/3} \sin \theta_i}{[(1 - \cos \theta_i)^2 (2 + \cos \theta_i)]^{1/3}} = 0.61 \left(\frac{We}{Oh} \right)^{0.166} \quad (21)$$

It is emphasized that in the approximate theory of the present section the spread-out contact angle θ_i plays the role of the receding contact angle; its value is close to 20° .

The potential energy available for drop receding from the spread-out shape is of the order of $F_r a_i$. If one neglects viscous dissipation during the receding motion (as shown above, this is possible in the present case), the height h at which the drop bounces is found from the energy balance $F_r a_i \approx mgh$, where m is the drop mass, and g is gravity acceleration. Using eqs 18–20 and the energy balance, we find the bouncing height of the drops as

$$h = K \frac{\gamma}{\rho g R_e} \left[0.61 \left(\frac{We}{Oh} \right)^{0.166} \right]^2 (\cos \theta_i - \cos \theta_{eV}) \quad (22)$$

where K is the dimensionless factor which is less than 1 to account for the viscous losses and the kinetic energy of the oscillatory motions in the bouncing drops. Note that, as shown above, the viscous losses are practically negligible in the present case and the value of K is predominantly determined by the

oscillatory motions in the bouncing drops. It is discussed in the following section. In eq 22 the angle θ_i is found from eq 21, and the angle θ_{eV} from eqs 14 and 15 in the case of the unstretched Teflon. In the case of the stretched Teflon, the only change is that eq 14 is replaced by eqs 16 and 17.

Equation 22 shows that as the voltage U increases, and thus the angle θ_{eV} decreases and $\cos \theta_{eV}$ increases, the height h decreases. The largest bouncing height is achieved at $V = 0$, when $\theta_{eV} = \theta_{e0}$ where in the cases of the unstretched and stretched Teflon, $\theta_{e0} = \theta_{e0, \text{unstretched}}$ or $\theta_{e0} = \theta_{e0, \text{stretched}}$, respectively. In the following section the predictions of eqs 14 (or 16 and 17 for the stretched Teflon), 15, 21, and 22 for the dependence $h = h(V)$ are compared to the experimental data in Figure 11.

4. RESULTS AND DISCUSSION

4.1. Hydrophobic to Superhydrophobic Conversion of Teflon. Among all solid organic polymers, poly(tetrafluoroethylene) (PTFE) is known to have the lowest surface energy.³⁶ PTFE, which is well-known as Teflon, shows hydrophobic and oleophilic characteristics. The hydrophobic properties of PTFE are caused by the fluorination of the carbon bonds. An equilibrium contact angle of water drops on the unstretched PTFE surface is about $108 \pm 2^\circ$.²⁹ The equilibrium contact angle of water drops can be dramatically raised by increasing the surface roughness of Teflon by its stretching. With increasing the stretching ratio parallel to the fibrous crystals of Teflon from 0 to 200%, the static water contact angle (SWCA) increases from $96 \pm 4^\circ$ to $147 \pm 5^\circ$ (Figure 6a) when observed in the direction orthogonal to that of the main surface ridges (Figures 7 and 8); that is, the surface changes its wetting properties from hydrophobic to superhydrophobic. The same conclusion is reached when the contact angle is observed in the direction parallel to the main surface ridges (Figure 6b and c). Note that the latter two figures show some effect of the surface anisotropy on the contact angle.

The change in surface roughness, i.e., the surface area ratio $r > 1$, associated with the change in the microstructure of the PTFE crystals due to stretching results in switching the surface wetting properties from hydrophobic (unstretched Teflon) to superhydrophobic (stretched Teflon). For the unstretched Teflon, the SWCA is $96 \pm 4^\circ$ (hydrophobic), whereas for the stretching of 50%, the SWCA dramatically changed to $125 \pm 5^\circ$ (ultrahydrophobic). For the stretching of 100–200%, the SWCA increases slowly from $139 \pm 3^\circ$ to $147 \pm 5^\circ$ (superhydrophobic).

To link the wettability change to the surface morphology, scanning electron microscope (SEM) images of the unstretched and stretched Teflon (200%) were taken (Figure 7). Teflon is a semicrystalline polymer, where the crystals are aligned in a regular parallel array of relatively intact ridges before stretching (Figure 7a). Some loosely bound PTFE fibers are clearly seen lying in between the ridges. When the Teflon tape is stretched, the forces to be overcome are not the strong chemical bonds in the polymer chains, but the van der Waals attractions between PTFE crystals. Compared with chemical bonds, van der Waals attractions are so weak that they can be easily overcome by stretching.³³ The SEM image (Figure 7b) shows that the stretched ridges are crisscrossed by microcracks resulting from stretching. This increases the surface area ratio r compared to the unstretched Teflon and is responsible for the superhydrophobicity. The three-dimensional surface topography images of the unstretched and stretched Teflon (200%)

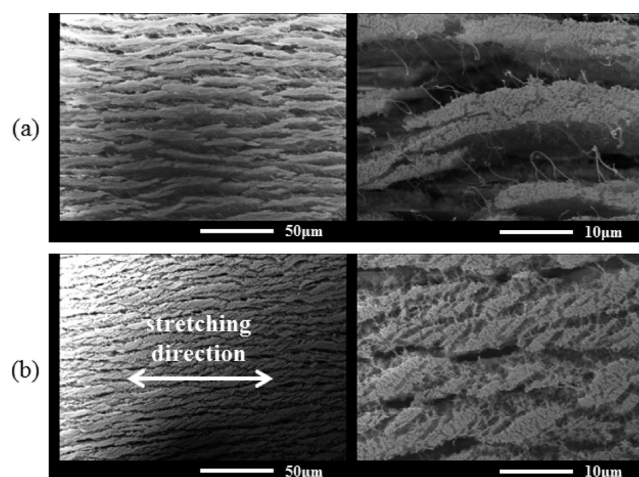


Figure 7. SEM images of Teflon surface (a) unstretched and (b) 200%-stretched. Multiple microcracks appear across the ridges in the stretched sample.

obtained by AFM are shown in Figure 8a,c and b,d, respectively.

The roughness of the unstretched Teflon measured by AFM was 209.9 nm (when measured using a $20 \times 20 \mu\text{m}^2$ sample) or 157.8 nm (when measured using a $5 \times 5 \mu\text{m}^2$ sample), whereas it was higher, 245.6 or 223.1 nm, respectively, in case of the stretched Teflon. The surface area ratio of the stretched Teflon found from eq 17 is also listed in Table 1.

4.2. Dynamic Electrowetting on Unstretched and Stretched Teflon. Drop impact tests with and without EW were performed to investigate the ability of the unstretched and stretched Teflon (200%) to repel or impale impacting water drops. During these experiments, various wetting regimes like, complete rebound, partial rebound, nonrebound, and deposition of drops were observed. In the absence of EW, with no voltage applied at 0 kV, for both the unstretched (Figure 9a) and stretched Teflon (Figure 10a) it was found that when a water drop impacts onto a surface, it first deforms and flattens into a pancake shape. After that, the receding motion begins when the radius of the pancake diminishes. Finally, a drop can rebound off the surface. The drop remains completely intact during the impact and does not break into smaller water droplets.

However, the rebounding heights h_{max} of water drops at $V = 0$ kV were different in the case of the unstretched and stretched Teflon (Figure 11a). The rebounding height was higher for the stretched Teflon ($h_{\text{max}} \approx 5.13$ mm) and lower for the unstretched one ($h_{\text{max}} \approx 4.16$ mm).

After applying a potential of 2 kV to the unstretched Teflon (Figure 9b), it was found that although the spreading process was similar to that at 0 kV (Figure 9a), the rebound changed and the drop separated into two parts. The rebound height at 2 kV ($h_{\text{max}} \approx 3$ mm) was diminished compared to the one at 0 kV ($h_{\text{max}} \approx 4.16$ mm). Then the voltage was systematically increased up to 6.0 kV. At 6.0 kV (Figure 9c), there was no rebound on the unstretched Teflon and the water drop stayed pinned to the surface having the equilibrium contact angle of $78 \pm 3^\circ$. So the voltage of 6.0 kV is considered to be the EW voltage for the unstretched Teflon. Hence, EW decreased the equilibrium water contact angle on the unstretched Teflon from $96 \pm 4^\circ$ to $78 \pm 3^\circ$ at the EW voltage of 6.0 kV.

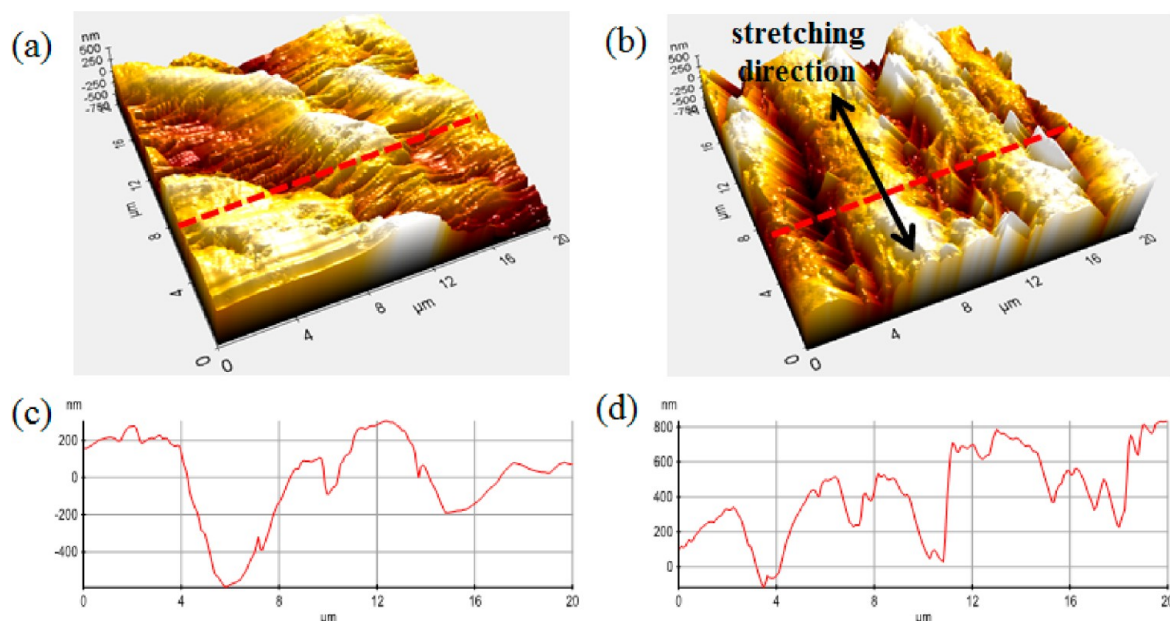


Figure 8. AFM images of Teflon surface (a) unstretched and (b) 200%-stretched. The surface profiling line is shown by the dashed red line. The surface elevations corresponding to the unstretched and stretched samples are shown in panels c and d, respectively.

Table 1. RMS Roughness (R_q) and the Surface Area Ratio r^a

	R_q [nm]		r
	$20 \times 20 \mu\text{m}^2$	$5 \times 5 \mu\text{m}^2$	
(a) unstretched	209.9	157.8	1
(b) 200%-stretched	245.6	223.1	8.0

^aThe averaged values of R_q were obtained using the data from 16 different areas.

After applying a potential of 2 kV to the stretched Teflon (Figure 10b) it was found that the impacting water drop spreads first, then recedes and rebounds off the surface, while a tiny part of it is still pinned to the surface. Even though the water drop rebounds off the surface, the rebound height is reduced from $h_{\text{max}} \approx 5.13$ mm at $V = 0$ kV to $h_{\text{max}} \approx 1.8$ mm at $V = 2$ kV (Figure 11a). At 3 kV (Figure 10c) water drops strongly stick to the surface without any rebound, so this voltage is considered as the EW voltage for the stretched

Teflon. Such water drops possess the equilibrium contact angle of $67 \pm 5^\circ$. Hence, EW decreased the water contact angle of the stretched Teflon from $147 \pm 5^\circ$ to $67 \pm 5^\circ$ at EW voltage of 3 kV. It is emphasized that the mutual orientation of the direction of stretching and the interelectrode direction on the Teflon surface had no effect on the results.

In comparison, a higher EW voltage (~ 6.0 kV) was required to reduce the equilibrium water contact angle on the unstretched Teflon from $96 \pm 4^\circ$ to $78 \pm 3^\circ$, and the corresponding hydrophobic to partially hydrophilic switching angle difference was only $18 \pm 4^\circ$. On the other hand, a comparatively lower EW voltage (~ 3 kV) was required to reduce the equilibrium water contact angle of the stretched Teflon from $147 \pm 5^\circ$ to $67 \pm 5^\circ$, and the superhydrophobic to partially hydrophilic switching angle difference was significantly larger $\sim 80 \pm 5^\circ$.

It is emphasized that the directional structure of the unstretched and stretched Teflon seen in Figures 7 and 8

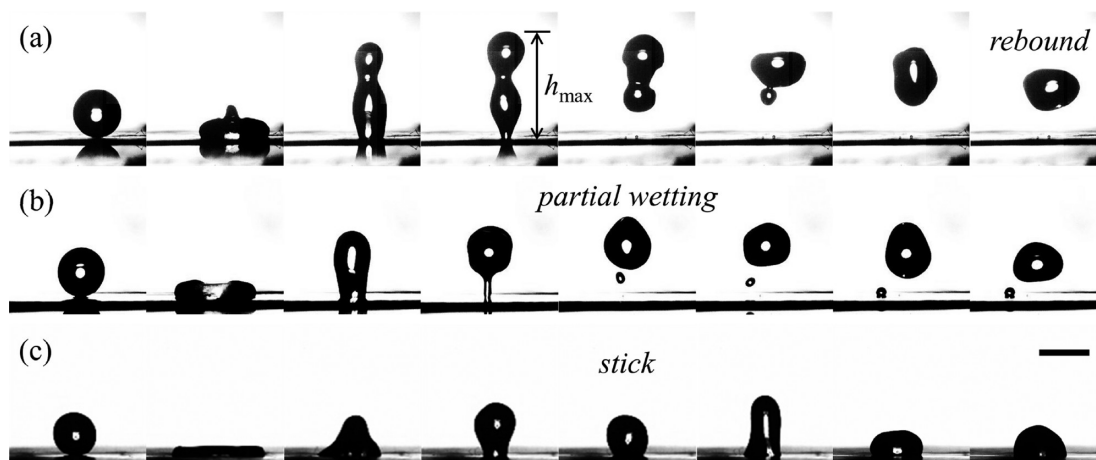


Figure 9. Snapshots of drop impact onto the unstretched Teflon at (a) $V = 0$ kV, (b) $V = 2$ kV, and (c) $V = 6.0$ kV. Time interval between the frames is 15 ms, and the scale bar is 2 mm. The corresponding videos are included in the Supporting Information (SI).

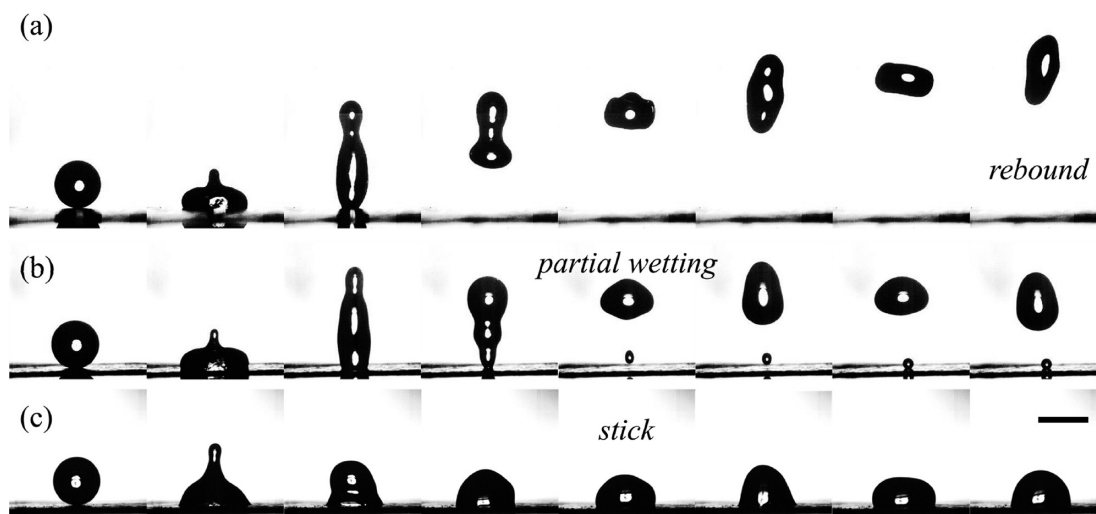


Figure 10. Snapshots of drop impact onto the 200%-stretched Teflon at (a) $V = 0$ kV, (b) $V = 2$ kV, and (c) $V = 3$ kV. Time interval between the frames is 15 ms, and the scale bar is 2 mm. The interelectrode line was parallel to the direction of the sample stretching. The corresponding videos are included in the SI.

does not have any significant effect on drop bouncing from these surfaces at any voltage applied, as the comparison of the results corresponding to the two orientations of the interelectrode line relative to the ridges reveals in Figure 11b. This is probably partially related to the fact that the static contact angle is also only weakly affected by the surface directionality, as Figures 6b,c show.

The theoretical predictions are compared to the experimental data in Figure 11a. The calculations were done with $We = 10.43$, $Oh = 0.0039$, $\epsilon = 2.1$, $\gamma = 70.76$ mN/m, $d = 100$ μ m, and $a/d = 2.60$ (for the unstretched Teflon), and $d = 70$ μ m and $a/d = 2.83$ (for the stretched Teflon). Also, it was taken $\rho = 1000$ kg/m³ and $R_e = 0.00096$ m, and assumed that the b/d is sufficiently large compared to a/d to have a negligible effect on the results (cf. eq 15). The dimensionless factor K in eq 22 was chosen as $K = 0.098$ for the impacts on the unstretched Teflon, and $K = 0.064$ for the impacts on the 200%-stretched Teflon. The values of K were determined from the corresponding cases when no voltage was applied and kept the same for the other cases (with voltage applied). They are of the same order of magnitude but the value of K for the 200%-stretched surface is lower than the one for the unstretched surface. This is presumably due to the fact that the rougher stretched surface slightly increases viscous losses, which are still small. The comparison of the experimental results with the predictions reveals a reasonable agreement. The values of K of the order of 0.1 show that only about 10% of the surface energy stored in the spread-out drop is spent for bouncing. The rest 90% are split between viscous losses (relatively small for water) and the kinetic energy of the vigorous drop oscillations in flight visible in the snapshots in Figures 9 and 10 and the corresponding videos in the SI.

Since viscous losses are negligible in the present case, as shown above, the value of K can be evaluated using the equation for the distribution of the supplied potential energy, namely

$$mgH = mgh + mV_{\text{osc}}^2 \quad (23)$$

where H is the height from which the original drop was released and V_{osc} is of the order of the magnitude of the oscillatory motion in the bounced drop. Then

$$K \approx \frac{h}{H} \approx 1 - \frac{V_{\text{osc}}^2}{V_0^2} \quad (24)$$

where use is made of the fact that V_0^2 is of the order of gH .

The analysis of the video recordings corresponding to Figures 9 and 10 reveals typical values of $V_{\text{osc}} \approx 0.59$ – 0.6 m/s in drops which bounced off the unstretched and stretched surfaces, while $V_0 = 0.62$ m/s. Then, according to eq 24, one obtains $K = 0.0635$ – 0.0944 , which is in a very good agreement with the values of $K = 0.064$ and 0.098 used in the theoretical predictions in Figure 11a.

5. CONCLUSION

The hydrophobic Teflon was converted into superhydrophobic Teflon by simply stretching it. The dynamic electrowetting (EW) studied in this work for the first time does not involve an electrode directly attached to the drop as in the case of the static EW. As a result, the capacitance is dramatically reduced in the present case and the EW phenomena can be observed only in a much higher voltage range (in the kV range instead of the V range) compared to the ordinary static electrowetting. A sharp EW response of the 200%-stretched Teflon was found experimentally and confirmed theoretically, with the full EW with the complete suppression of rebound of water drops achieved at the voltage of 3 kV. Correspondingly, the equilibrium contact angle was changed from $147 \pm 3^\circ$ (superhydrophobic) at $V = 0$ kV to $67 \pm 5^\circ$ (partially hydrophilic) at 3 kV. The EW response was weaker for the unstretched Teflon, with the full EW with the complete suppression of rebound of water drops achieved at the voltage of 6.0 kV. Correspondingly, the equilibrium contact angle was changed from $96 \pm 4^\circ$ to $78 \pm 3^\circ$ at 6.0 kV. The simplified theory of the dynamic electrowetting proposed in this work was capable of predicting the experimental data with reasonable accuracy.

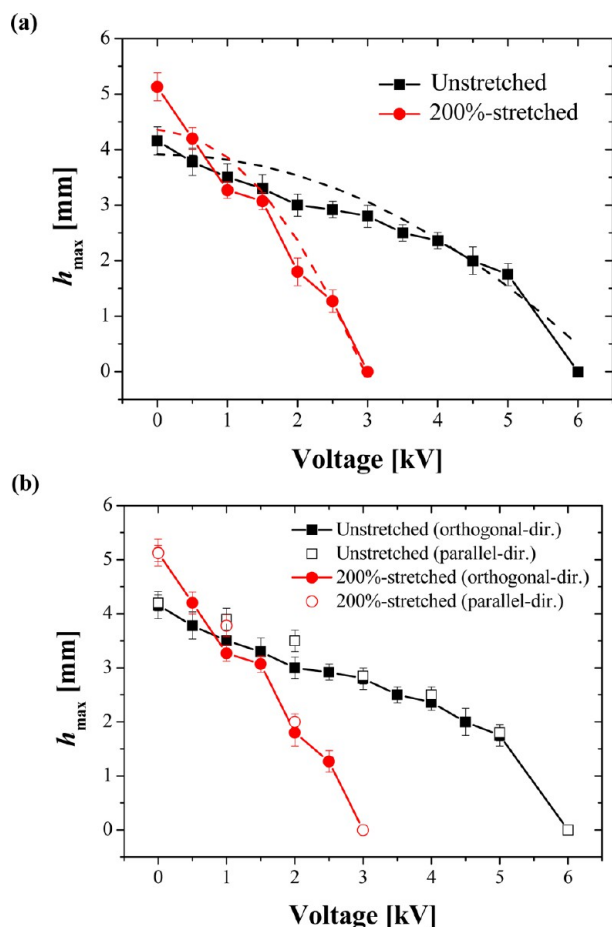


Figure 11. Maximum rebound height of a drop after impact onto the unstretched and 200%-stretched Teflon surfaces. The experimental data are shown by symbols spanned by solid lines (black or open squares for the unstretched Teflon, and red or open circles for the stretched one). (a) The interelectrode line was in the direction orthogonal to the main ridges seen in Figures 7 and 8. The theoretical predictions are shown by dashed lines. For the unstretched surface $K = 0.098$ and for the 200%-stretched one, $K = 0.064$. (b) The data sets acquired with the interelectrode line orthogonal to the direction of the main ridges seen in Figures 7 and 8 (filled symbols) and in the direction of the main ridges seen in Figures 7 and 8 (open symbols).

■ ASSOCIATED CONTENT

Supporting Information

Corresponding videos for Figures 9 and 10. This material is available free of charge via the Internet at <http://pubs.acs.org>.

■ AUTHOR INFORMATION

Corresponding Author

*E-mail: ayarin@uic.edu; skyoona@korea.ac.kr.

Notes

The authors declare no competing financial interest.

■ ACKNOWLEDGMENTS

This work was supported by National Research Foundation (2011-0030433) and Human Resources Development of KETEP (2012-4030-200-120).

■ REFERENCES

- (1) Wong, T. S.; Kang, S. H.; Tang, S. K. Y.; Smythe, E. J.; Hatton, B. D.; Grinthal, A.; Aizenberg, J. Bioinspired self-repairing slippery surfaces with pressure-stable omniphobicity. *Nature* **2011**, *477*, 443–447.
- (2) Karniadakis, G.; Beskok, A.; Aluru, N. *Microflows and Nanoflows. Fundamentals and Simulation*; Springer: New York, 2005.
- (3) Yarin, L. P.; Mosyak, A.; Hetsroni, G. *Fluid Flow, Heat Transfer and Boiling in Micro-Channels*; Springer: New York, 2009.
- (4) Beni, G.; Hackwood, S.; Jackel, J. L. Continuous electrowetting effect. *Appl. Phys. Lett.* **1982**, *40*, 912–914.
- (5) Zhao, Y.; Cho, S. K. Micro air bubble manipulation by electrowetting on dielectric (EWOD): transporting, splitting, merging and eliminating of bubbles. *LChip* **2007**, *7*, 273–280.
- (6) Hayes, R. A.; Feenstra, B. J. Video-speed electronic paper based on electrowetting. *Nature* **2003**, *425*, 383–385.
- (7) Welters, W. J. J.; Fokkink, L. G. J. Fast electrically switchable capillary effects. *Langmuir* **1998**, *14*, 1535–1538.
- (8) Garrod, R. P.; Harris, L. G.; Schofield, W. C. E.; McGettrick, J.; Ward, L. J.; Teare, D. O. H.; Badyal, J. P. S. Mimicking a Stenocara beetle's back for microcondensation using plasmachemical patterned superhydrophobic–superhydrophilic surfaces. *Langmuir* **2006**, *23*, 689–693.
- (9) Kuiper, S.; Hendriks, B. H. W. Variable-focus liquid lens for miniature cameras. *Appl. Phys. Lett.* **2004**, *85*, 1128–1130.
- (10) Yang, S.; Krupenkin, T. N.; Mach, P.; Chandross, E. A. Tunable and latchable liquid microlens with photopolymerizable components. *Adv. Mater.* **2003**, *15*, 940–940.
- (11) Dubois, P.; Marchand, G.; Fouillet, Y.; Berthier, J.; Douki, T.; Hassine, F.; Gmouh, S.; Vaultier, M. Ionic liquid droplet as e-microreactor. *Anal. Chem.* **2006**, *78*, 4909–4917.
- (12) Shapiro, B.; Moon, H.; Garrell, R. L.; Kim, C. J. Equilibrium behavior of sessile drops under surface tension, applied external fields, and material variations. *J. Appl. Phys.* **2003**, *93*, 5794–5811.
- (13) Kilaru, M. K.; Heikenfeld, J.; Lin, G.; Mark, J. E. Strong charge trapping and bistable electrowetting on nanocomposite fluoropolymer: BaTiO₃ dielectrics. *Appl. Phys. Lett.* **2007**, *90*, 212906.
- (14) Fan, S. K.; Yang, H. P.; Wang, T. T.; Hsu, W. Asymmetric electrowetting—moving droplets by a square wave. *LChip* **2007**, *7*, 1330–1335.
- (15) Vallet, M.; Vallade, M.; Berge, B. Limiting phenomena for the spreading of water on polymer films by electrowetting. *Eur. Phys. J.* **1999**, *11*, 583–591.
- (16) Wang, K. L.; Jones, T. B. Saturation effects in dynamic electrowetting. *Appl. Phys. Lett.* **2005**, *86*, 054104.
- (17) Krupenkin, T. N.; Taylor, J. A.; Schneider, T. M.; Yang, S. From rolling ball to complete wetting: the dynamic tuning of liquids on nanostructured surfaces. *Langmuir* **2004**, *20*, 3824–3827.
- (18) Wang, Z.; Ci, L.; Chen, L.; Nayak, S.; Ajayan, P.; Koratkar, N. Polarity-dependent electrochemically controlled transport of water through carbon nanotube membranes. *Nano Lett.* **2007**, *7*, 697–702.
- (19) Han, Z.; Tay, B.; Tan, C.; Shakerzadeh, M.; Ostrikov, K. Electrowetting control of Cassie-to-Wenzel transitions in superhydrophobic carbon nanotube-based nanocomposites. *ACS Nano* **2009**, *3*, 3031–3036.
- (20) Zhu, L.; Xu, J.; Xiu, Y.; Sun, Y.; Hess, D. W.; Wong, C. Electrowetting of aligned carbon nanotube films. *J. Phys. Chem. B* **2006**, *110*, 15945–15950.
- (21) He, B.; Patankar, N. A.; Lee, J. Multiple equilibrium droplet shapes and design criterion for rough hydrophobic surfaces. *Langmuir* **2003**, *19*, 4999–5003.
- (22) Lembach, A.; Tan, H. B.; Roisman, I. V.; Gambaryan-Roisman, T.; Zhang, Y.; Tropea, C.; Yarin, A. L. Drop impact, spreading, splashing and penetration in electrospun nanofiber mats. *Langmuir* **2010**, *26*, 9516–9523.
- (23) Sinha-Ray, S.; Zhang, Y.; Yarin, A. L. Thorny devil nano-textured fibers: The way to cooling rates of the order of 1 kW/cm². *Langmuir* **2011**, *27*, 215–226.
- (24) Weickgenannt, C. M.; Zhang, Y.; Lembach, A. N.; Roisman, I. V.; Gambaryan-Roisman, T.; Yarin, A. L.; Tropea, C. Non-isothermal drop impact and evaporation on polymer nanofiber mats. *Phys. Rev. E* **2011**, *83*, 036305.

- (25) Weickgenannt, C. M.; Zhang, Y.; Sinha-Ray, S.; Roisman, I. V.; Gambaryan-Roisman, T.; Tropea, C.; Yarin, A. L. The inverse-Leidenfrost phenomenon on nanofiber mats on hot surfaces. *Phys. Rev. E* **2011**, *84*, 036310.
- (26) Sahu, R.; Sinha-Ray, S.; Yarin, A. L.; Pourdeyhi, B. Drop impacts on electrospun nanofiber membranes. *Soft Matter* **2012**, *8*, 3957–3970.
- (27) Cassie, A. B. D.; Baxter, S. Wettability of porous surfaces. *Trans. Faraday Soc.* **1944**, *40*, 546–551.
- (28) Wenzel, R. N. Resistance of solid surfaces to wetting by water. *Ind. Eng. Chem.* **1936**, *28*, 988–994.
- (29) Youngblood, J. P.; McCarthy, T. J. Ultrahydrophobic polymer surfaces prepared by simultaneous ablation of polypropylene and sputtering of poly(tetrafluoroethylene) using radio frequency plasma. *Macromolecules* **1999**, *32*, 6800–6806.
- (30) Mugele, F.; Baret, J.-C. Electrowetting: from basics to applications. *J. Phys.: Condens. Matter* **2005**, *17*, 705–774.
- (31) Yarin, A. L. Drop impact dynamics: splashing, spreading, receding, bouncing. *Annu. Rev. Fluid Mech.* **2006**, *38*, 159–192.
- (32) Scheller, B. L.; Bousfield, D. W. Newtonian drop impact with a solid surface. *AIChE J.* **1995**, *41*, 1357–1367.
- (33) Reznik, S. N.; Yarin, A. L.; Theron, A.; Zussman, E. Transient and steady shapes of droplets attached to a surface in strong electric fields. *J. Fluid Mech.* **2004**, *516*, 349–377.
- (34) Russel, W. B.; Saville, D. A.; Schowalter, W. R. *Colloidal Dispersions*; Cambridge University Press: Cambridge, U.K., 1989.
- (35) Polya, G.; Latta, G. *Complex Variables*; Wiley: New York, 1974.
- (36) Bernett, M. K.; Zisman, W. A. Wetting properties of tetrafluoroethylene and hexafluoropylene copolymers. *J. Phys. Chem. B* **1960**, *64*, 1292–1294.